remote sensing

MDPI

Article

Spatiotemporal Dynamics of Tree Species-Level Aboveground Carbon Storage at the Canal Scale Under Green Engineering with a Random Forest Model

Wenhuan Wang [1], Wenqian Wu [1], Wei Zhang [1], Dongdong Hu [2], Weifeng Xu [3], Jie Bai [4] and Yinghui Wang [1,5,*]

[1] School of Marine Sciences, Guangxi University, Nanning 530004, China; wwhuan@st.gxu.edu.cn (W.W.); wuwenqian@st.gxu.edu.cn (W.W.); zhangwei20@gxu.edu.cn (W.Z.)
[2] Guangxi Forest Inventory & Planning Institute, Nanning 530011, China; hdd2202@126.com
[3] School of Resources, Environment and Materials, Guangxi University, Nanning 530004, China; xwf@st.gxu.edu.cn
[4] School of Resources and Environment, University of Electronic Science and Technology of China, Chengdu 611731, China; baijie@uestc.edu.cn
[5] Institute of Green and Low Carbon Technology, Guangxi Institute of Industrial Technology, Nanning 530200, China
* Correspondence: wyh@gxu.edu.cn

Highlights

What are the main findings?

- A 10 m species-level aboveground carbon (AGC) mapping framework was developed coupling Sentinel-1/2 and the random forest (RF) algorithm, enabling fine-scale carbon monitoring during canal construction.
- Total AGC decreased by 16.88%, dominated by losses from *Eucalyptus grandis*, yet the rebound of *Pinus massoniana*, carbon gain of *Litchi chinensis* and other native species effectively offset 34.45% of the carbon loss in the buffer area.

What are the implications of the main findings?

- Spatial AGC patterns reveal the Environmental Impact Area (EIA) as the disturbance core, while the Ecological Buffer Area (EBA) functioned as a carbon stabilizer, guiding targeted restoration planning.
- This study provides quantitative evidence for green engineering efficacy and supports SDG 15 by enabling precise monitoring of low-carbon infrastructure.

Abstract

Monitoring spatiotemporal dynamics of aboveground carbon (AGC) storage at the tree species level is crucial for evaluating the ecological impacts of large-scale infrastructure projects and facilitating accurate ecological environmental management. However, existing studies heavily rely on interannual coarse-spatial-resolution forest-type products, leading to significant uncertainties in carbon estimation, particularly in fragmented linear engineering zones. This study integrated Sentinel-1/2 data with a random forest (RF) model to map tree species distribution (overall accuracy = 85.18%; Kappa = 0.8319) and AGC estimation (R^2 = 0.7057; RMSE = 13.35 Mg ha^{-1}) at a 10 m resolution in the Pinglu Canal Basin from 2019 to 2024. The results revealed a total AGC decline of 16.88% across the watershed. Spatially, the Environmental Impact Area (EIA) functioned as the primary disturbance core (experiencing a 28.91% loss), while the Ecological Buffer Area (EBA) acted as a regional carbon stabilizer. At the species level, while *Eucalyptus grandis* accounted for the majority of carbon depletion, *Pinus massoniana* exhibited a resilience-driven rebound in the mid-construction phase. Meanwhile, *Litchi chinensis* and other native species demonstrated

Check for updates

Academic Editors: Hubert Hasenauer and Liming He

Received: 19 November 2025
Revised: 18 January 2026
Accepted: 27 January 2026
Published: 2 February 2026

Copyright: © 2026 by the authors. Licensee MDPI, Basel, Switzerland. This article is an open access article distributed under the terms and conditions of the Creative Commons Attribution (CC BY) license.

steady gains. Cumulatively, these species-specific carbon gains associated with natural growth and restoration initiatives effectively offset 34.45% of the carbon loss. These findings provide quantitative evidence supporting the potential of green engineering to mitigate the ecological footprint of infrastructure development. This study offers a robust monitoring tool for low-carbon infrastructure and directly supports the United Nations Sustainable Development Goal 15 (SDG 15) related to forest conservation and ecological restoration.

Keywords: aboveground carbon storage; tree species level; green engineering; random forest; multi-source remote sensing fusion; Pinglu Canal

1. Introduction

Forests represent the largest carbon reservoir in terrestrial ecosystems, storing approximately 50% of terrestrial carbon and playing a vital role in mitigating climate change [1,2]. Quantifying the dynamics of aboveground carbon (AGC) serves as the fundamental basis for evaluating ecosystem service functions and represents a critical scientific issue in analyzing the mechanism through which human activities influence the ecological environment [3]. The United Nations Sustainable Development Goal 15 (Life on Land) plays a crucial role in promoting sustainable forest management, averting biodiversity loss, and rehabilitating degraded landscapes. This goal is of great significance in tackling the urgent environmental challenges confronted at present. However, rapid infrastructure expansion continues to destroy forest composition and deplete carbon stocks through vegetation clearance and soil disturbance [4]. Especially for riparian zones and canals, which are linear ecosystems with heterogeneous geomorphic units, construction causes the forest ecosystem to experience rapid and complex structural changes. The measure of green engineering, integrating ecological restoration into infrastructure design and construction, has therefore emerged as a key pathway to reconcile development with carbon neutrality goals [5]. Yet, dynamic change in forest carbon under the influence of green engineering, particularly at the tree species level, remains poorly quantified. The Pinglu Canal Project in southern China represents a flagship case of green engineering [6,7]. This project integrates ecological slope protection, native forest restoration, and riparian vegetation rehabilitation, creating a unique ecological experiment for studying the carbon dynamics of forest ecosystems under the combined disturbances of engineering construction and ecological restoration in linear infrastructure.

Traditional approaches to estimating forest carbon stocks primarily rely on destructive field sampling and allometric equations, which are labor-intensive and spatially discontinuous [8,9]. In recent decades, rapid advancements in remote sensing technologies have revolutionized AGC estimation, enabling consistent, high-resolution mapping at regional to global scales [10]. Optical sensors such as Landsat and Sentinel-2 provide information on canopy reflectance and vegetation indices (e.g., NDVI, EVI, and NBR) to infer biomass and carbon storage, but they are limited by cloud contamination, atmospheric interference, and spectral saturation in dense canopies, which can reduce the accuracy of biomass estimation in subtropical forests. Radar sensors (e.g., Sentinel-1 or ALOS PALSAR) can penetrate cloud cover and complement optical data by capturing canopy structure, allowing all-weather and continuous AGC monitoring [11], yet their performance can be affected by speckle noise and topographic effects. Airborne and spaceborne Light Detection and Ranging (LiDAR) missions (e.g., GEDI or ICESat-2) offer direct measurements of canopy height and vertical structure [12], but the high cost and sparse coverage of LiDAR data also constrain large-scale applications [13]. Recent studies emphasize multi-source data fusion, integrat-

ing optical, radar, and LiDAR datasets to leverage their complementary strengths [14,15]. The fusion of Sentinel-1 Synthetic Aperture Radar (SAR) with Sentinel-2 multispectral data effectively mitigates the saturation limitations of optical indices, while LiDAR provides critical vertical structural information that enhances model accuracy [16]. Furthermore, multi-source fusion faces challenges related to sensor resolution inconsistency and data pre-processing complexity. Because different remote sensing techniques possess advantages and limitations, the integration of these techniques, along with their combination with direct ground measurements and topographic data, is integral for optimizing the accuracy and precision of carbon estimations across space and time.

Machine learning techniques, which operate without strictly pre-defined functional forms, have been extensively applied in various fields such as land use classification, tree species identification, and remote sensing inversion [17–19]. These techniques exhibit superiority in discerning complex pattern associations between carbon variables and spatial–spectral characteristics through adaptive learning processes [20]. They showed substantial potential for advancing inversion modeling in carbon estimation like random forest (RF) [21–23], K Nearest Neighbors (KNN) [24,25], and Extreme Gradient Boosting (XGBoost) [26,27]. In contrast, RF exhibits the capability to process multi-source data, demonstrates robustness in the face of noise and overfitting, and shows insensitivity to multicollinearity through its random feature subspace mechanism [28]. The proven advantages of RF algorithms in terms of accuracy and reliability have positioned them as the most extensively adopted and favored approach for evaluating aboveground carbon storage through remote sensing. Although the integration of remote sensing data and machine learning algorithms presents notable advantages in large-scale carbon stock estimating, this approach has limitations in generating spatially detailed estimations of forest carbon storage.

It should be noted that when integrating forest carbon estimation with forest type identification and classification datasets, the complementary advantages of these two aspects can be comprehensively utilized to generate aboveground carbon stock estimations at the tree species level. However, many studies often simply divide the study area into forest and non-forest areas relying on some already-existing and public land cover products [29], or classify forests only into broad functional types (e.g., broadleaf, coniferous, or mixed broadleaf–conifer forest) rather than species-level taxonomy [30]. Significant disparities in carbon sequestration capacity among tree species [31], coupled with variations in growth characteristics, biomass distribution, and disturbance resistance, result in remarkably different carbon responses under disturbance [32,33]. For canal construction, accurate species-level AGC estimation offers crucial insights for precisely evaluating carbon storage changes under engineering projects and formulating effective carbon management strategies.

To address the absence of refined species classification and carbon assessment in linear infrastructure zones, this study aims to conduct fine-scale monitoring and quantify the dynamic changes in forest carbon under green engineering initiatives. By synergizing Sentinel-2 multispectral data and Sentinel-1 SAR with the RF algorithm, the specific research objectives are to (a) accurately map the spatial distribution of dominant tree species within the Pinglu Canal Basin at a 10 m resolution; (b) quantify the spatiotemporal evolution of aboveground carbon stocks across three construction phases (pre-construction in 2019, early construction in 2022, and mid-construction in 2024) and two distinct spatial scales (the Environmental Impact Area [EIA] and the Ecological Buffer Area [EBA]); and (c) assess the specific contributions of diverse tree species to carbon recovery and evaluate the effectiveness of green engineering. Ultimately, this research provides quantitative evidence supporting the development of low-carbon infrastructure and offers scientific guidance for sustainable canal management.

2. Materials and Methods

2.1. Study Area

The Pinglu Canal is located in Guangxi, China, with a total length of 134.2 km. It starts from Pingtang Estuary of Xijin Reservoir area, Hengzhou City, Nanning, flows through Lingshan County, and enters Beibu Gulf via Qinjiang River. The Pinglu Canal is the first canal project connecting river and sea in China since 1949 and is also the land–sea ecological corridor in the west district of China (Figure 1). The geographical position of the buffer zone covers 108°32′–109°04′E and 21°44′–22°39′N. The overall topography of the canal watershed slopes downward from north to south. Elevation ranges from 47 m below sea level to 371 m above sea level, resulting in a maximum north–south elevation difference of approximately 400 m. The construction of the canal commenced in 2022, and it is anticipated to be officially opened for navigation by the end of 2026. The watershed encompasses diverse land cover types, including built-up areas, water bodies, cropland, grassland, and forest. Forests are dominant as the primary land cover type, making up approximately 34% of the watershed area (according to the 2019 official forest inventory statistics), and they play a crucial role in regulating the local ecological environment and microclimate. The main forest types are evergreen broadleaved and needle-leaved forests, composed of four main tree species, namely, *Eucalyptus grandis*, *Pinus elliottii*, *Pinus massoniana*, and *Litchi chinensis*, and other trees representing over thirty species.

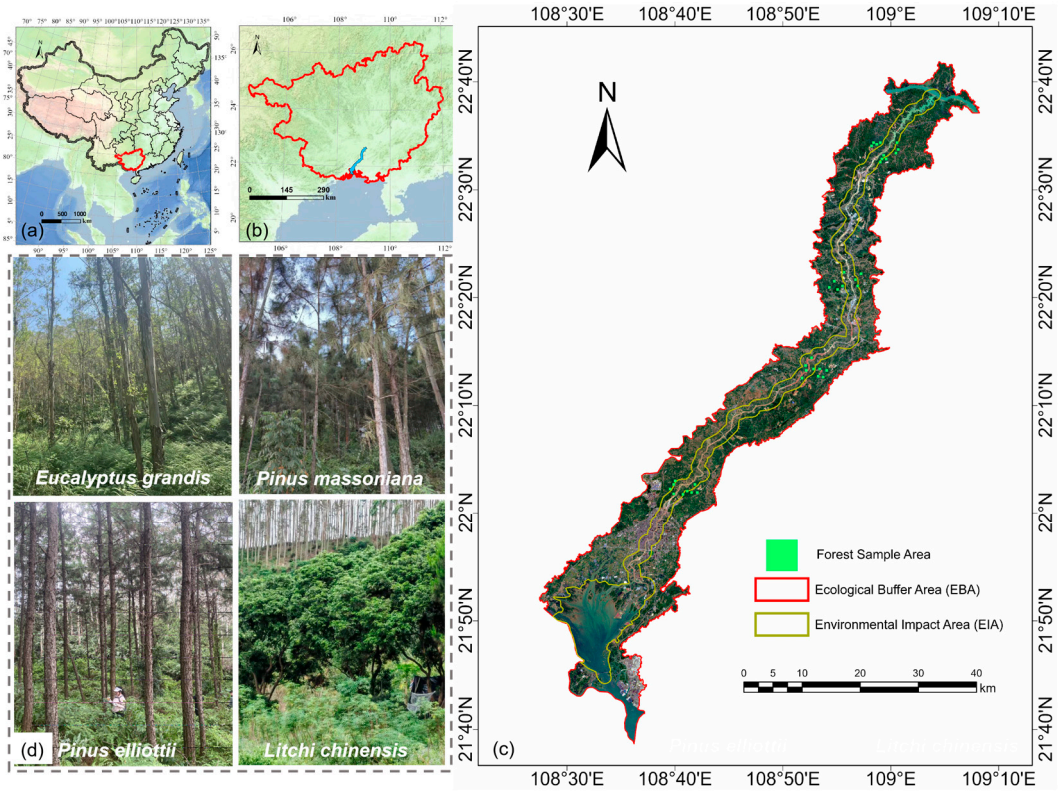


Figure 1. Geographical overview of the study area and field survey details. (**a**) Location of the Guangxi Zhuang Autonomous Region within China. (**b**) Location of the Pinglu Canal Basin within Guangxi. (**c**) Detailed spatial distribution of the study area, delineating the Ecological Buffer Area (EBA) (red boundary) and the Environmental Impact Area (EIA) (yellow boundary). Green markers indicate the distribution of forest sampling areas. (**d**) Representative field sample plots of the dominant tree species.

The canal project operates under a core mandate of ecological respect and conservation priority. The "green engineering" concept integrates strategic measures to safeguard and en-

hance forest carbon sinks, encompassing ecological restoration, compensatory afforestation, and resource circularity. These actions collectively reinforce the resilience of the regional forest carbon pool. The construction of the Pinglu Canal commenced in 2022, with multiple ecological restoration projects being carried out simultaneously alongside canal development, including forest compensation covering 2884.66 hectares, ecological slope protection spanning 322.78 hectares, and landscape greening covering 22.41 hectares. As of October 2024, approximately 50% of the ecological restoration projects have been completed. This area provides an ideal study area for exploring the evolution of tree-species-level AGC at the canal scale under green engineering initiatives.

To explicitly assess the gradient of engineering impacts and carbon dynamics, the study area was spatially stratified into two functional zones. The Environmental Impact Area (EIA) is defined as a linear corridor that extends 1 km on either side of the canal. It represents the core disturbance zone exposed to direct engineering activities, including channel excavation, embankment construction, and infrastructure development. The Ecological Buffer Area (EBA) encompasses the broader hydrological catchment surrounding the canal, functioning as a regional ecological barrier and a comparative background for evaluating ecosystem stability. The boundaries were demarcated based on hydrological principles, utilizing the HydroSHEDS watershed dataset (hybas_as_lev12_v1c) and the pour point dataset (hybas_pour_lev12_v1_shp). Watershed extraction was carried out using the Watershed Tool in ArcGIS Pro (Version 3.0, Esri, Redlands, CA, USA).

2.2. Datasets

2.2.1. Satellite Imagery Acquisition and Processing

The end of the growth period (September and October), when forest biomass reaches its annual peak, is generally considered optimal for monitoring and assessing forest growth conditions. Harmonized Sentinel-2/MSI Level-2A surface reflectance imageries were acquired on the Google Earth Engine (GEE) platform from September to October in 2019, 2022, and 2024. Subsequently, cloud detection was performed on the remote sensing imageries for these two months in three years using the QA60 and MSK_CLDPRB index layers. Following cloud detection, a median composite imagery was generated from all available dates. Nine multispectral bands were collected, including 10 m resolution bands (B2, B3, B4, and B8) and 20 m resolution bands (B5, B6, B7, B8A, and B11). The 20 m resolution bands were then resampled to 10 m spatial resolution with cubic convolution interpolation.

In addition, Sentinel-1 Ground Range Detected (GRD) data were acquired on the same dates. The data, acquired in Interferometric Wide Swath mode with dual polarization (VH and VV) at C-band (5.3 GHz) via the GEE platform, had a 10 m resolution and an average incidence angle of 37.6. All polarimetric data were converted to backscattering coefficients, ranging from 0 to 1. Together with the multispectral imagery, all datasets were reprojected to the Albers Equal-Area Conic projection to facilitate subsequent area calculations within the study region. The integration of distinct physical dimensions, including optical spectra, SAR structural backscatter, and topographic variables, provides unique information, guaranteeing the comprehensive capture of complex, nonlinear vegetation dynamics.

2.2.2. Field Data Collection

Field measurements of forest structure parameters were conducted from September to October 2024. The forest survey, as illustrated in Figure 1, involved 37 square plots, each measuring 25 m $\times$ 25 m. These plots were distributed from the canal's upstream to its estuary and were surveyed between September and October 2024, encompassing the full tree species diversity known in the study area. Within each plot, tree structural parameters were measured, including diameter at breast height (DBH), tree height (H), and

tree species. Additionally, a handheld Real-Time Kinematic (RTK) device (E93, CHCNAV, Shanghai, China) was employed to record the geographic coordinates of every tree measured for structural parameters within each plot, benefiting the high-precision matching with satellite imagery.

The Forest Resources Management (FRM) imagery is a multi-objective cyclic inventory for national and large-scale assessment of forest resources [34]. The imagery attains an accuracy of up to 0.0001 hectares, with a precision exceeding 95%, which is acquired through the cross-verification of multi-source data, encompassing high-resolution satellite images, high-precision unmanned aerial vehicle (UAV) images, the National Land Resource Survey, and ground field surveys. The FRM data of Guangxi in 2019 were employed to generate training and testing samples through visual interpretation to delineate tree species categories and diverse land cover for the subsequent random forest classification.

2.3. Methods

2.3.1. Overall Technique Flowchart

This study proposes an integrated framework for carbon storage estimation at the canal scale, with the detailed technical workflow illustrated in Figure 2. The framework comprises three core components: (1) dataset acquisition and processing, (2) refined tree species classification, and (3) carbon storage mapping. Methodologically, multispectral Sentinel-2 images from September to October in the years 2019, 2022, and 2024 were collected. Cloud detection was performed using the QA60 band and S2 cloud probability product, followed by median compositing. The composited data were uniformly resampled to 10 m spatial resolution and reprojected to the Albers equal-area conic (AEAC) projection to ensure precise pixel-area calculations. Additionally, Sentinel-1 VV and VH polarimetric data for the same period were median-composited and identically reprojected to the AEAC projection. For carbon storage modeling at the pixel scale, structural parameters, including tree height, diameter at breast height (DBH), and species of over 4000 individual trees, were utilized. Meanwhile, species-level training samples for random forest classification were generated from Forest Resources Monitoring (FRM) imagery, enabling quantitative analysis of carbon storage changes at the tree species level in the canal region.

2.3.2. Feature Extraction

Drawing upon extensive previous research in forest remote sensing [14,35], it is established that optimal classification and carbon storage inversion do not require an exhaustive list of indices but rather a curated set of physically representative variables. While multispectral indices are fundamental, excessive feature input can significantly increase computational burden and complexity without necessarily improving model outcomes. This study adopted a strategic feature selection approach, prioritizing 14 key variables that have proven effective in capturing distinct biophysical properties of vegetation in heterogeneous landscapes.

These features integrate complementary information sources. The raw surface reflectance (eight bands) and vegetation indices (NDVI) capture spectral and phenological traits [36]. The normalized difference built-up index (NDBI) and water index (NDWI) distinguish non-forest targets. The digital elevation model (DEM) represents environmental gradients, and the dual-polarization SAR products (VV and VH) provide vertical structural information [11,37]. This multi-source configuration theoretically suffices for tree species discrimination and carbon estimation requirements while minimizing redundancy. Specifically, the 14 key feature inputs into the random forest model include the raw surface reflectance for eight bands, NDVI, NDBI, NDWI, DEM, and Sentinel-1 VV/VH backscatter, as detailed in Table 1. It should be noted that Band 11 was mainly acquired for

the calculation of spectral indices (NDBI) and was not utilized as an independent feature in the model.

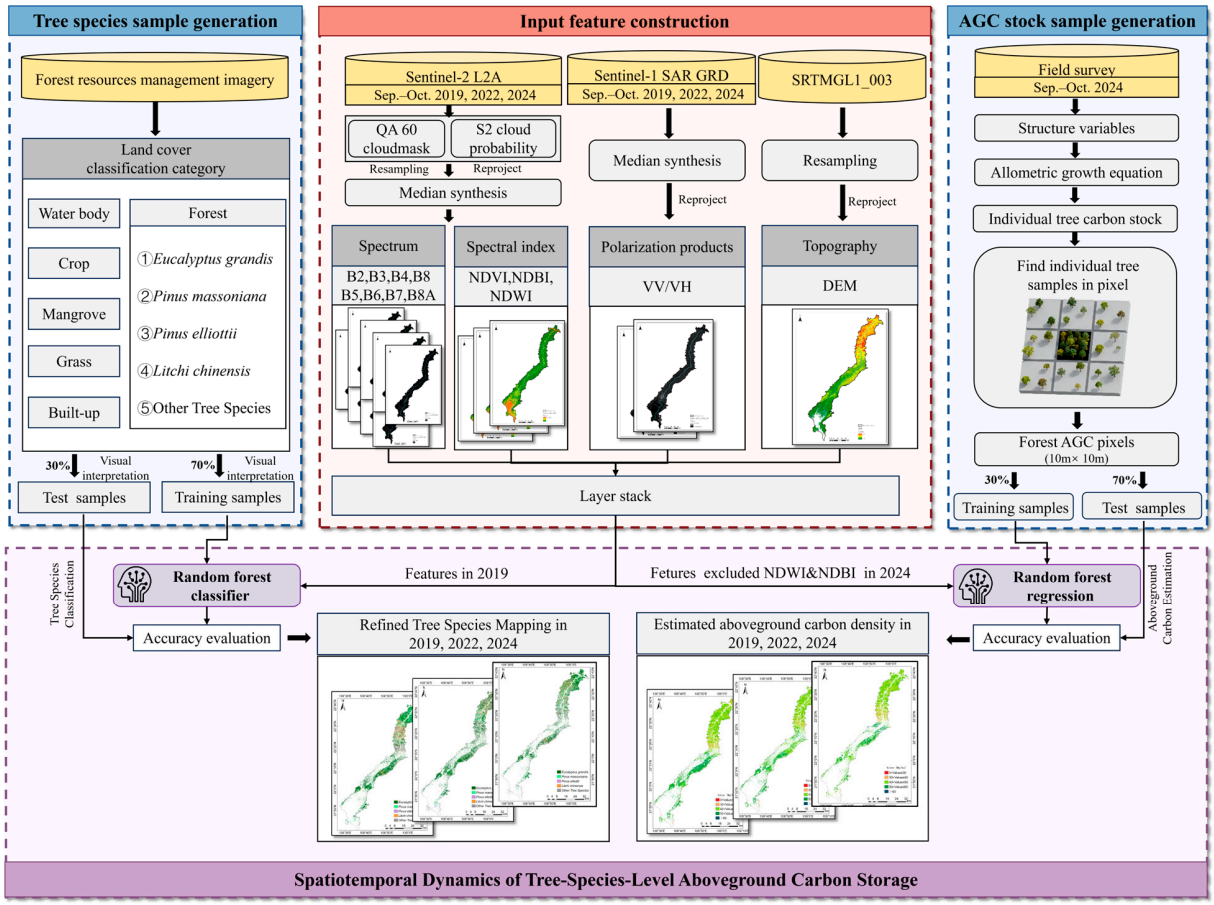


Figure 2. The overall technical flowchart of this study. The framework is structured into four main processes: tree species sample generation, input feature construction, AGC stock sample generation, and spatiotemporal analysis. Colored dashed boxes demarcate these processing stages, while arrows indicate the sequential data flow.

Table 1. Lists of predictors utilized for tree species classification modeling.

Data Category	Data Products	Predictor	Definition/Formulation
Multispectral imagery data	Sentinel-2 L2A	Band 2	Blue, central wavelength (CWL): 490 nm Spatial resolution (SR): 10 m
		Band 3	Green (G), CWL: 560 nm, SR: 10 m
		Band 4	Red (R), CWL: 660 nm, SR: 10 m
		Band 5	Red Edge 1, CWL: 705 nm, SR: 20 m
		Band 6	Red Edge 2, CWL: 740 nm, SR: 20 m
		Band 7	Red Edge 3, CWL: 782 nm, SR: 20 m
		Band 8	Near-Infrared (NIR), CWL: 835 nm, SR: 10 m
		Band 8A	Red Edge 4, CWL: 842 nm, SR: 20 m
Polarimetric data	Sentinel-1 GRD	VV	Vertical emission—vertical receipt
		VH	Vertical emission—horizontal receipt
DEM	/	SRTMGL1_003	SR: 30 m, free available
Spectral index data	/	NDVI	(NIR − R)/(NIR + R)
		NDBI	(SWIR − NIR)/(SWIR + NIR); Short-wavelength infrared (SWIR), Band 11, SR: 20 m
		NDWI	(G − NIR)/(G + NIR)

2.3.3. Random Forest Algorithm

In this research, the random forest (RF) algorithm was employed for both tree species classification and aboveground carbon (AGC) regression modeling. RF is a non-parametric ensemble learning method based on bootstrap aggregating (Bagging), which trains multiple decision trees on random subsets of data to reduce variance and overfitting [38]. Although the core architecture remains consistent, the mathematical principles for node splitting differ between the two tasks. For tree species classification, the algorithm utilizes the Gini Impurity index to measure the quality of a split; the final class label is determined by majority voting across all trees. For AGC estimation regression, the algorithm employs the Least Squares Deviation (Variance Reduction) criterion to minimize the prediction error; the final AGC value is derived by averaging the outputs of individual trees.

The models were implemented on the GEE platform by utilizing the ee.Classifier.smileRandomForest API. To ensure experimental consistency and computational efficiency, identical hyperparameter settings were applied to both the classification and regression models. The cross-validation with a 50% overlap verified that the optimal quantity of random forest trees is 100; when the quantity surpasses 100, the model accuracy reaches a stable state. Bag fraction was set to 0.5, meaning that 50% of the data was randomly sampled to train each tree, while the remaining data were used to ensure model diversity and reduce overfitting. Variables per split was set to the default value (null), which corresponds to the square root of the total number of input features, ensuring randomness in feature selection. Minimum leaf population was set to 1, allowing the trees to grow fully to capture fine-grained variations. Finally, output mode was specifically set to classification for species mapping and regression for carbon stock estimation.

2.3.4. Refined Tree Species Mapping Method

To enhance the reliability of tree species classification, this study employs Forest Resources Monitoring (FRM) imagery of the canal region for sample calibration. The canal region was classified into 10 major land cover categories: five refined tree species within forested zones (*Eucalyptus grandis*, *Pinus massoniana*, *Pinus elliottii*, *Litchi chinensis*, and an "other tree species" class encompassing over 20 additional species based on field surveys), supplemented by five non-forest classes (mangroves, water bodies, built-up areas, cropland, and grassland). For each category, sample points were systematically manually annotated with the following maximum counts: *Eucalyptus grandis* (2000), *Pinus massoniana* (2000), *Pinus elliottii* (936), *Litchi chinensis* (1138), other tree species (2000), mangrove (645), built-up (2000), water body (2000), cropland (2000), and grassland (2000). Corresponding 14 feature values were extracted for each sample point to establish complex nonlinear mappings between pixel characteristics and classification labels. In addition, sample points were partitioned with 70% allocated for training the random forest classification model and 30% reserved for the validation of classification accuracy. A confusion matrix was employed to assess the classification outcomes, and the model achieved an overall classification accuracy of 85.18% and a Kappa coefficient of 0.8319 (Table 2), indicating high consistency between the classification results and the validation data.

Table 2. The confusion matrix of our random forest classification framework.

True/ Predicted	*Eucalyptus grandis*	*Pinus massoniana*	*Pinus elliottii*	*Litchi chinensis*	Other Tree Species	Mangrove	Built -Up	Water Body	Cropland	Grassland	Producer Accuracy
Eucalyptus grandis	532	27	4	11	29	0	4	0	10	2	0.8595
Pinus massoniana	33	496	15	5	18	2	3	2	4	1	0.8566
Pinus elliottii	10	37	190	8	14	0	1	0	1	0	0.7280
Litchi chinensis	20	10	2	267	16	0	3	0	5	2	0.8215
Other tree species	31	30	4	25	463	1	11	2	16	1	0.7928
Mangrove	0	0	0	0	0	181	0	5	5	0	0.9476

Table 2. *Cont.*

True/ Predicted	*Eucalyptus grandis*	*Pinus massoniana*	*Pinus elliottii*	*Litchi chinensis*	Other Tree Species	Mangrove	Built -Up	Water Body	Cropland	Grassland	Producer Accuracy
Built-up	1	2	0	0	2	0	522	18	27	0	0.9126
Water body	1	2	0	0	4	2	18	535	13	0	0.9304
Cropland	7	4	0	2	19	2	38	24	482	2	0.8310
Grassland	0	0	0	0	8	1	6	3	18	91	0.7165
User accuracy	0.8378	0.8158	0.8837	0.8396	0.8080	0.9577	0.8614	0.9083	0.8296	0.9192	/
Overall accuracy: 85.18%; Kappa coefficient: 0.8319											

2.3.5. Carbon Stock Estimation Model

The forest vegetation carbon storage calculated in this study focuses on the aboveground part, excluding the underground, soil, and litter layer. Accurate estimation of forest aboveground carbon (AGC) storage at the pixel level relies on precise geometric alignment between field-measured individual tree data and remote sensing imagery. A prevalent source of error in remote sensing inversion is the edge effect, which involves the erroneous inclusion of pixels intersecting plot boundaries. In the case of these edge pixels, the satellite sensor records the spectral information across the entire pixel area. Conversely, the field survey only measures the biomass of trees situated within the plot line (excluding unmeasured trees immediately outside the boundary). This disparity results in a systematic underestimation of biomass in relation to spectral predictors. To rigorously address this issue, we adopted a strict spatial matching strategy using high-precision RTK coordinates. A pixel was defined as a valid pixel only if its spatial extent fell entirely within the boundary of the 25 m × 25 m sample plot. This ensures that every tree contributing to the pixel's reflectance was measured and accounted for in the biomass calculation. Edge pixels were systematically excluded to prevent noise introduction. Based on this geometric criterion, the extracted valid pixels typically corresponded to the representative core areas of the forest stands.

Following the identification of valid pixels, the aboveground biomass (AGB) of individual trees was calculated using species-specific allometric equations. Depending on the models available in the literature [39], either a one-variable or two-variable model was applied:

$$AGB_{tree} = a \times DBH^b \times H^c \quad (1)$$

$$AGB_{tree} = a \times DBH^b \quad (2)$$

where AGB_{tree} represents aboveground biomass per tree (kg), DBH denotes diameter at breast height (cm), and H indicates tree height (m). The specific coefficients applied for each dominant species are detailed in Table 3.

Table 3. Allometric equation coefficients and carbon conversion factors for dominant tree species.

Tree Species	Equation Model	Parameter a	Parameter b	Parameter c	Carbon Factor (f_C)
Eucalyptus grandis	$a \times DBH^b$	0.1746	2.333	-	0.5253
Pinus massoniana	$a \times DBH^b \times H^c$	0.06662	2.09317	0.49763	0.5254
Pinus elliottii	$a \times DBH^b \times H^c$	0.04744	2.10359	0.63108	0.4756
Litchi chinensis	$a \times DBH^b$	0.1875	2.333	-	0.4834

Following the calculation of individual tree biomass, aboveground carbon storage per tree (AGC_{tree}) was derived by applying species-specific carbon conversion factors (f_C):

$$AGC_{tree} = AGB_{tree} \times f_C \quad (3)$$

Subsequently, pixel-level carbon storage was calculated by aggregating individual tree carbon values within each valid pixel:

$$AGC_{pixel} = \sum_{i=1}^{n} AGC_{tree,i} \quad (4)$$

where AGC_{pixel} represents aboveground carbon storage of the valid pixel. $AGC_{tree,i}$ denotes the i-th individual tree carbon stock within the pixel (where i = 1, . . ., n), and n signifies the total number of trees contained within the pixel.

This process establishes a quantitative linkage between pixel-level and individual tree-level carbon storage, enabling precise alignment of field-measured tree structural parameters with remote sensing pixels, while ensuring reliable aboveground carbon estimation at the pixel scale. Subsequently, referring to previous research, 12 key features commonly used and with established physical relevance to vegetation carbon dynamics were extracted from all valid pixels for random forest regression modeling, including eight bands of raw surface reflectance, VV/VH polarization features, NDVI, and DEM. Notably, this study intentionally employs a streamlined feature set—empirically justified and theoretically sound—to achieve robust inversion performance. Variables such as NDWI and NDBI were excluded from carbon modeling due to their lack of physical correlation with forest AGC based on remote sensing physical principles, despite their historical use in previous multi-feature inversion frameworks.

The determination coefficient (R^2) and root mean square error (RMSE) were used to evaluate the performance and accuracy of the random forest regression model. Calculation formulas of the relevant indicators are given as Equations (5) and (6).

$$R^2 = 1 - \frac{\sum_{i=1}^{n}(y_i - \hat{y}_i)^2}{\sum_{i=1}^{n}(y_i - \overline{y})^2} \quad (5)$$

$$RMSE = \sqrt{\frac{\sum_{i=1}^{n}(\hat{y}_i - y_i)^2}{n}} \quad (6)$$

where y_i and $\hat{y}_i$ denote the true values and retrieved carbon stock values, respectively. $\overline{y}$ is the average of true carbon stock values, and n is the number of pixels.

Data visualization and statistical graphing were performed using Origin (Version 2024, OriginLab Corporation, Northampton, MA, USA).

3. Results

3.1. Refined Tree Species Mapping and Distribution Characters

Based on the established classification model, tree species classification of the Pinglu Canal area was carried out for the years 2019, 2022, and 2024. Adhering to consistent protocols for remote sensing data acquisition and pre-processing, the multi-year remote sensing data were transformed into raster datasets with the same spatial resolutions and row–column numbers. The remote-sensing feature variables required for the model were extracted, and finally, tree species classification was performed based on the RF model. The refined tree species classification maps (Figure 3) and forest change maps (Figure 4) revealed pronounced spatial–temporal variations in forest coverage and tree species distribution across the basin.

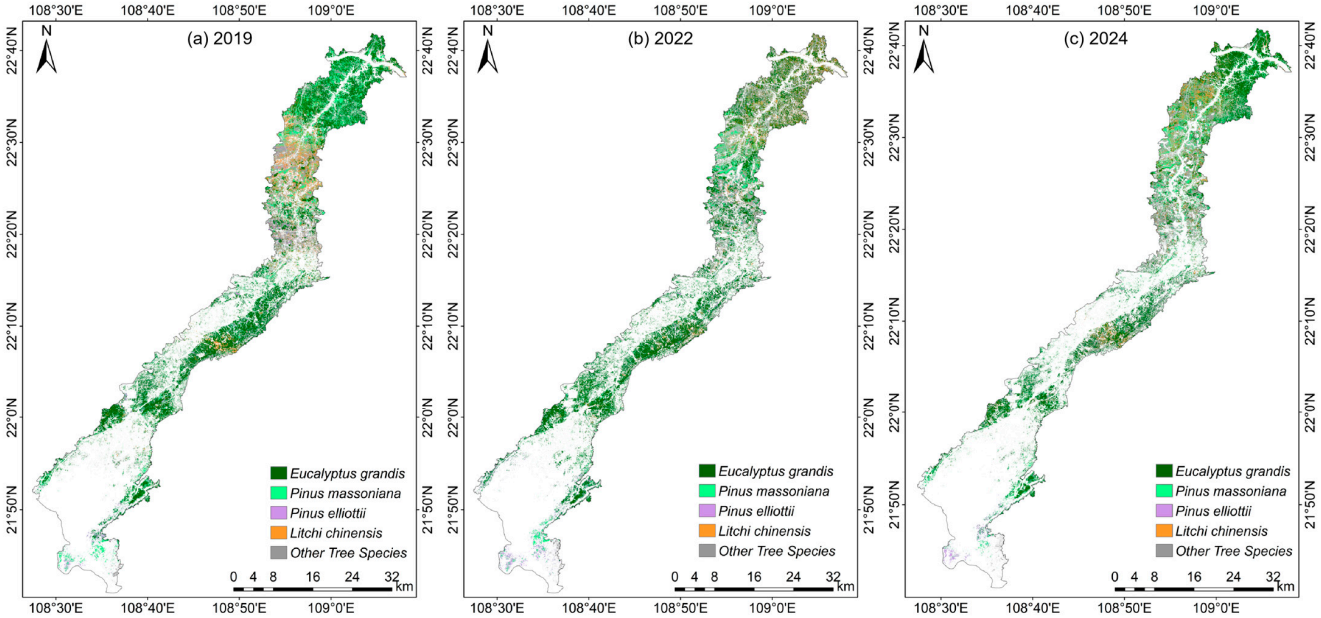


Figure 3. Spatiotemporal distribution of refined tree species in the Pinglu Canal Basin across three phases: (**a**) pre-construction in 2019, (**b**) early construction in 2022, and (**c**) mid-construction in 2024.

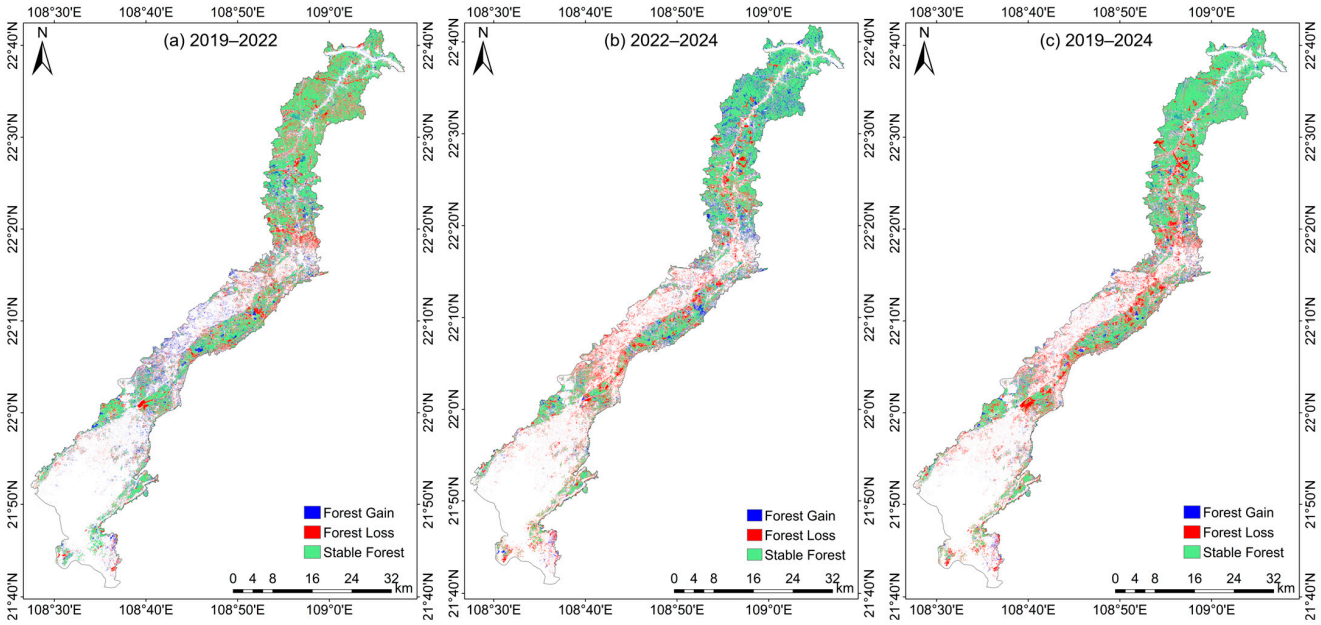


Figure 4. Spatiotemporal distribution of forest dynamics in the Pinglu Canal Basin. The maps display changes during the early construction phase ((**a**): 2019–2022), the mid-construction phase ((**b**): 2022–2024), and the overall period ((**c**): 2019–2024). Red regions indicate forest loss, blue regions indicate forest gain, and green regions represent stable forest cover.

Spatially, the vegetation dynamics equally exhibited distinct regional heterogeneity. The northern hilly region experienced frequent landscape fragmentation. As shown in Figure 3, large patches of *Eucalyptus grandis* present in 2019 transitioned to non-forest or other tree species in 2022, and partially recovered by 2024. To differentiate these rapid shifts from potential model instability, verified representative transition pixels were referenced against high-resolution historical imagery. This confirmed that inherent classification errors may contribute to minor random noise; the observed large-scale shifts predominantly reflect real land use changes, including the short-rotation harvesting cycles of *Eucalyptus* plantations and temporary land occupation for construction. The central canal corridor

(within the EIA) showed a distinct linear pattern of permanent forest loss. A continuous "white belt" of non-forest area emerged along the north–south axis in 2022 and 2024, cutting through the landscape due to channel excavation. However, along the edges of this corridor, scattered patches of *Pinus massoniana* densified in 2024, indicating early ecological restoration. The middle region, dominated by *Litchi chinensis* orchards, maintained high spatiotemporal stability throughout the study period. Unlike the harvested timber forests, these economic fruit forests were consistently managed and preserved.

Table 4 presents the forest area in the canal basin. In the Ecological Buffer Area (EBA), where forest cover experienced moderate fluctuations between 2019 and 2024, before construction (2019), the total forest area reached 54,932.02 ha, dominated by *Eucalyptus grandis* (42.20%, 23,178.77 ha) and *Pinus massoniana* (20.91%, 11,489.05 ha). *Litchi chinensis* and *Pinus elliottii* contributed 9.62% and 4.42%, while other tree species occupied 12,550.33 ha (22.85%). During 2019–2022, the total forest area declined to 49,755.86 ha (−9.42%), predominantly in sub-catchments spatially corresponding to temporary access roads and soil disposal sites. *E. grandis* and *P. massoniana* decreased by 15.65% and 38.04%, respectively, while *L. chinensis* and other tree species expanded by 14.52% and 17.44%. In 2024, the forest area further decreased to 46,584.20 ha (−15.20%). *E. grandis* remained dominant but decreased to 16,685.50 ha (−28.0%), whereas *L. chinensis* and other species increased by 10.52% and 8.50%, coinciding with reforestation and compensatory planting initiatives. Forest distribution transformed from a relatively homogeneous plantation matrix into a more heterogeneous structure.

Table 4. Forest area within the Ecological Buffer Area (EBA) and Environmental Impact Area (EIA) from 2019 to 2024.

Tree Species	EBA (ha)			EIA (ha)		
	2019	2022	2024	2019	2022	2024
Eucalyptus grandis	23,178.77	19,550.40	16,685.50	3126.13	3210.83	2068.23
Pinus massoniana	11,486.38	7116.60	9066.46	2088.15	1351.47	1626.98
Pinus elliottii	2429.36	2295.16	1371.15	413.17	497.49	201.59
Litchi chinensis	5287.18	6055.11	5843.60	1001.74	758.46	585.47
Other tree species	12,550.33	14,738.59	13,617.49	2166.80	2212.22	1907.16
Total	54,932.02	49,755.86	46,584.20	8795.99	8030.47	6389.43

In the Environment Impact Area (EIA), the forest area totaled 8795.99 ha in 2019, mainly *E. grandis* (35.54%, 3126.13 ha) and *P. massoniana* (23.70%, 2085.94 ha). *L. chinensis* and *P. elliottii* contributed 11.39% and 4.70%, with other tree species covering 2166.80 ha (24.64%). By 2022, the forest area decreased to 8030.47 ha (−8.70%), corresponding to vegetation clearance along the canal corridor. *P. massoniana* declined sharply (−35.28%). In 2024, the total forest area experienced a substantial decline, reaching 6389.43 ha, representing a decrease of 27.36%. The areas of *E. grandis*, *P. elliottii*, and *L. chinensis* all exhibited significant reductions. In contrast, the area of *P. massoniana* increased by 20.39%. This result shows that the EIA experienced more intense disturbance and slower recovery and the vegetation maintained a spatially fragmented pattern.

3.2. Spatial Characteristics of Aboveground Carbon Storage

Leveraging field-measured individual tree data and remote sensing imagery, a model was constructed to estimate aboveground carbon (AGC) stock. Figure 5 presents the inversion accuracy and error metrics, revealing that the model achieved an R^2 of 0.7057 and an RMSE of 13.35 Mg ha^{-1}, confirming the proposed feature composition's feasibility and ensuring reliable data support for subsequent aboveground carbon storage spatial–temporal analyses.

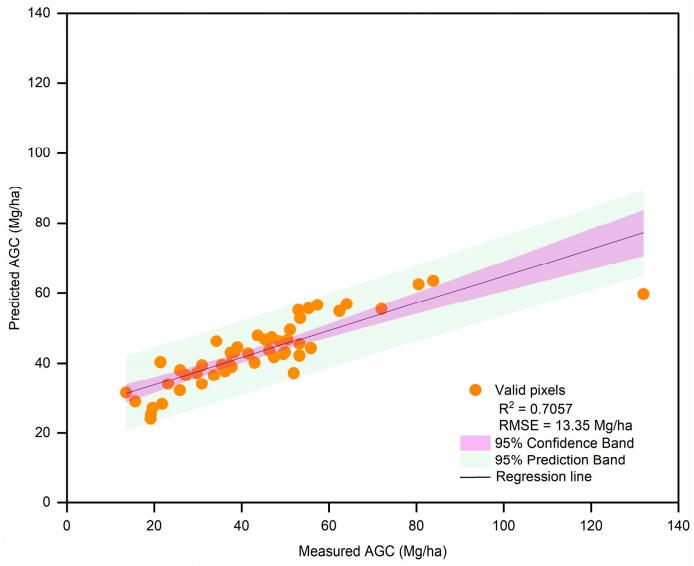


Figure 5. Scatter distribution of predicted AGC and measured AGC with the random forest regression model.

The spatial distribution (Figure 6) and dynamic changes (Figure 7) of AGC stocks were mapped across the Pinglu Canal Basin. In the Ecological Buffer Area (EBA), AGC stocks exhibited a continuous declining trend over the study period. As shown in Table 5, the total AGC decreased from 2.82 × 10^6 Mg in 2019 to 2.34 × 10^6 Mg in 2024, representing a cumulative loss of 16.88%. The mean AGC density changed slightly from 51.29 Mg ha^{-1} to 50.27 Mg ha^{-1}, remaining relatively stable throughout the observation period. Spatially, high-density carbon zones (>50 Mg ha^{-1}) remained relatively stable in the southern sectors, acting as a regional carbon reservoir. However, localized carbon reductions were observed in the central plains and sub-catchments, spatially aligning with temporary access roads and soil disposal sites. From 2022 to 2024, scattered patches of increasing AGC density emerged, presenting patterns consistent with initial biomass accumulation associated with ecological compensation projects, although their spatial extent remained fragmented.

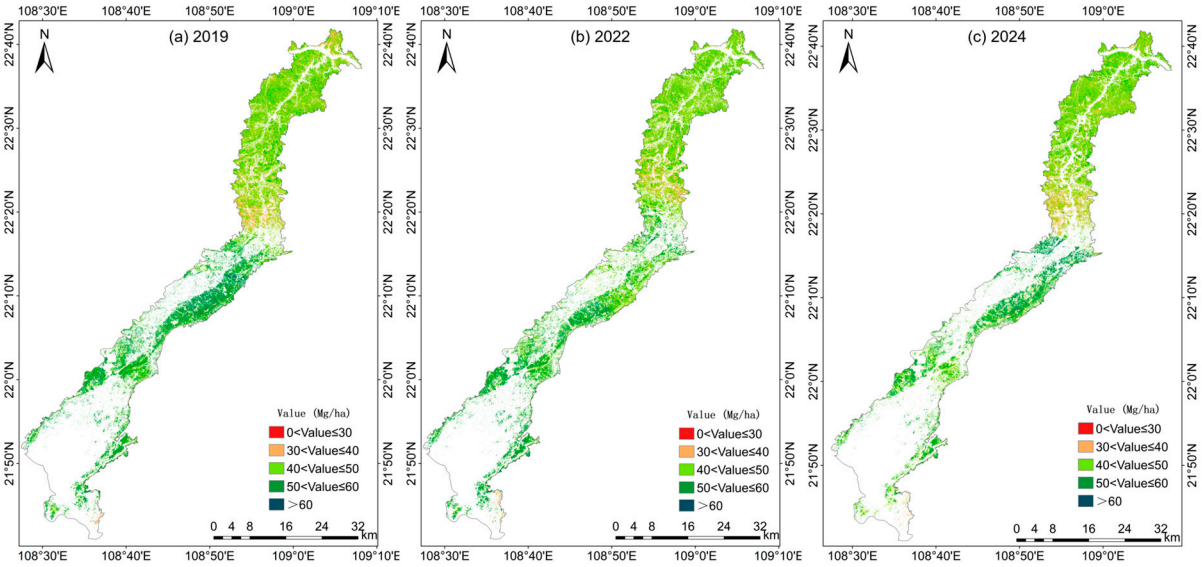


Figure 6. Spatiotemporal distribution of AGC density in the Pinglu Canal Basin across three phases: (**a**) pre-construction in 2019, (**b**) early construction in 2022, and (**c**) mid-construction in 2024.

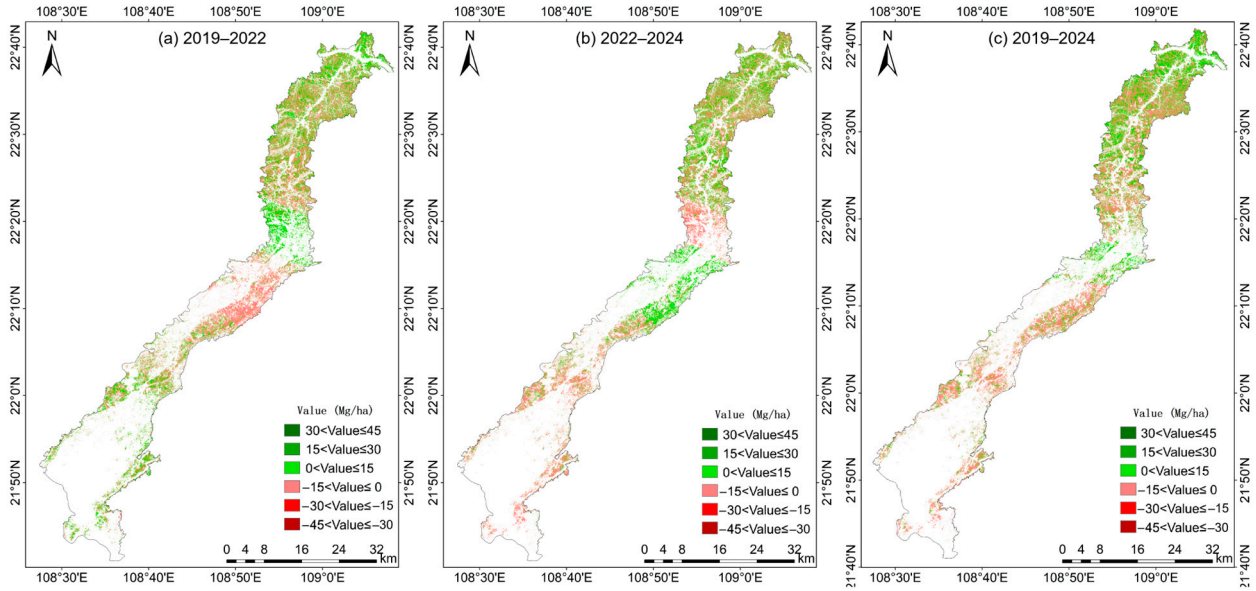


Figure 7. Spatial distribution of AGC change during the construction phases ((**a**): 2019–2022; (**b**): 2022–2024) and the overall period ((**c**): 2019–2024). The color gradient signifies the magnitude of change; green shades denote carbon gain (positive change), whereas red shades denote carbon loss (negative change).

Table 5. AGC and rate of AGC change from 2019 to 2024.

Area	AGC (Mg)			Rate of AGC Change (%)		
	2019	2022	2024	2022–2019	2024–2022	2024–2019
EBA	2,817,465.51	2,554,916.11	2,341,779.61	−9.32%	−8.34%	−16.88%
EIA	411,023.91	375,311.27	292,176.64	−8.69%	−22.15%	−28.91%

In the Environmental Impact Area (EIA), the carbon dynamics were markedly more drastic. The total AGC declined by 8.69% during the early construction phase (2019–2022) and plummeted by 22.15% in the mid-construction phase (2022–2024). Consequently, the cumulative carbon loss reached 28.91% by 2024 (4.11×10^5 Mg down to 2.92×10^5 Mg), significantly higher than EBA. Spatially, a distinct linear belt of concentrated carbon depletion was observed running through the central canal corridor. This pattern exhibits a high degree of spatial consistency with the engineering footprint, particularly in areas of intensive channel excavation and embankment construction. Conversely, in specific embankment sections, localized recovery trends were detected in 2024, spatially aligning with the areas designated for ecological slope protection. The mean AGC density slightly decreased from 46.73 Mg ha^{-1} to 45.73 Mg ha^{-1}, and remained lower in the EIA compared to surrounding buffer areas. This persistent disparity highlights the influence of topographic constraints and human activities on carbon distribution. The EIA naturally follows low-lying alluvial plains and riparian corridors, areas characterized by intensive agricultural activity, human settlement, and fragmented forest patches. In contrast, the EBA encompasses mountainous headwaters and contiguous forests with higher biomass accumulation potential. The difference underscores that the EIA represents a disturbed ecosystem where carbon stocks are inherently limited by landscape fragmentation.

3.3. Variation in Aboveground Carbon Storage by Tree Species

The Sankey diagrams (Figure 8) reveal interannual flows and compositional shifts in AGC stocks for dominant tree species. In the EBA (Figure 8a), *E. grandis* remained the dom-

inant carbon carrier but experienced a continuous decline, dropping from 1.26 × 10^6 Mg in 2019 to 8.80 × 10^5 Mg in 2024. This species was the primary contributor to the cumulative carbon loss (7.26 × 10^5 Mg), mainly affected by short rotation cutting in plantations. Similarly, *P. elliottii* followed a downward trajectory, shrinking significantly from 1.28 × 10^5 Mg to 7.13 × 10^4 Mg, further exacerbating the loss of coniferous plantation stocks. The other tree species category exhibited a fluctuating pattern, peaking in 2022 (7.06 × 10^5 Mg) before declining, yet remaining a substantial component of the regional carbon pool. In contrast, *P. massoniana* exhibited a distinct recovery trajectory: after a sharp decline in 2022, it rebounded to 4.66 × 10^5 Mg in 2024. Along with the stability of *L. chinensis*, this indicates that the carbon gain (2.50 × 10^5 Mg) was primarily driven by the growth and restoration of native coniferous and broadleaved species. Consequently, from 2019 to 2024, the cumulative carbon gain effectively offset 34.45% of the cumulative carbon loss at the species level in the EBA.

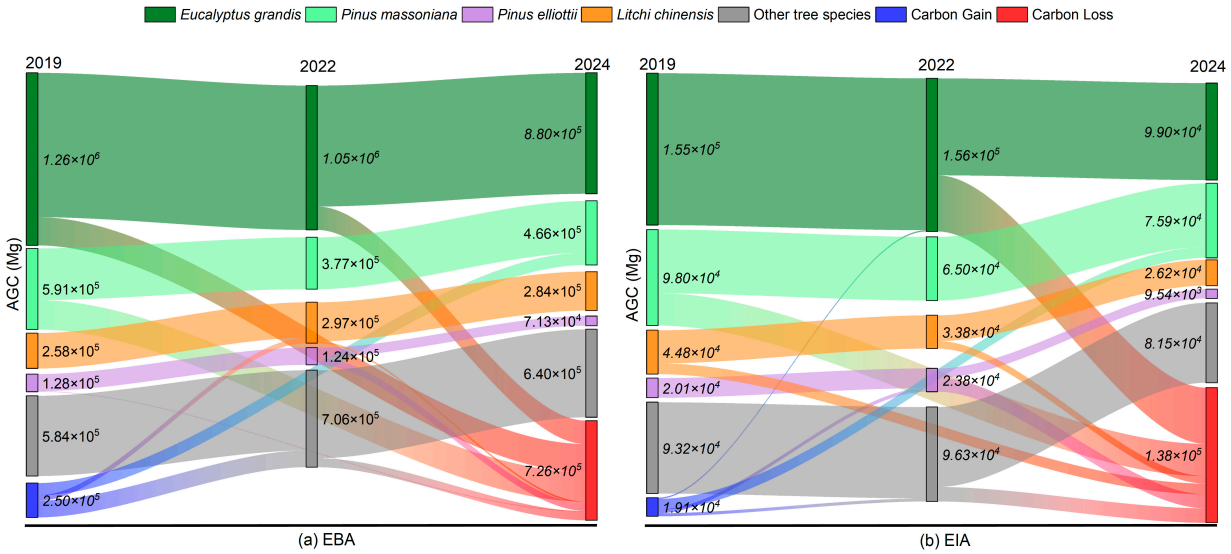


Figure 8. Interannual changes and compositional shifts in AGC stock within the (**a**) the Ecological Buffer Area (EBA) and (**b**) the Environmental Impact Area (EIA) from 2019 to 2024. The width of the flows is proportional to the carbon stock magnitude (Unit: Mg). The Carbon Gain and Carbon Loss nodes represent the cumulative gross flows of carbon accumulation and reduction across the two intervals (2019–2022 and 2022–2024), respectively.

In the EIA (Figure 8b), the carbon dynamics were more acutely aligned with the construction phases. *E. grandis* stocks remained relatively stable during the early phase (2019–2022) but suffered a precipitous drop in the mid-construction phase, falling to 9.90 × 10^4 Mg in 2024. This timing coincides with the intensification of channel excavation activities. *P. elliottii* faced severe depletion by 2024 (9.54 × 10^3 Mg). Conversely, *P. massoniana* demonstrated a recovery, rising to 7.59 × 10^4 Mg in 2024. This upward trend temporally corresponds to the implementation of ecological slope protection and greening initiatives along the canal banks. However, due to the intensity of engineering disturbance, the cumulative carbon loss in the EIA reached 1.38 × 10^5 Mg, substantially outweighing the carbon gain (1.91 × 10^4 Mg), reflecting the profound structural reshaping of the forest ecosystem in the core engineering zone.

In general, the compositional transformation from *Eucalyptus*-dominated monocultures to a diversified structure encompassing *Pinus*, *Litchi*, and other species indicates a functional reconfiguration of the carbon pool. In this process, the losses resulting from commercial timber extraction and construction are partially offset by the restoration of more stable native communities.

4. Discussion

4.1. Reliability, Transferability, and Uncertainty of the Framework

This study established a random forest-based coupled framework for the Pinglu Canal, enabling the quantitative evaluation of forest carbon dynamics at a refined species level. The reliability of this framework is fundamentally anchored in its physically interpretable feature selection strategy. Unlike previous studies that struggled with computational inefficiency due to high-dimensional inputs [40,41], 14 variables were prioritized based on their direct biophysical relevance. Regarding the potential redundancy among raw spectral bands, strict variable elimination was not implemented. Instead, the algorithmic robustness of random forest was leveraged through its random feature subspace mechanism. Furthermore, the integration of distinct physical dimensions including optical spectra (physiology), SAR backscatter (structure), and topography (environment) provided complementary information essential for capturing nonlinear vegetation dynamics.

This multi-source synergy was empirically validated by the classification performance. While distinguishing between spectrally similar coniferous species (*Pinus massoniana* and *Pinus elliottii)* presented a challenge using optical data alone, the incorporation of SAR texture and DEM allowed the model to discern nuanced differences in canopy structure and ecological niches. Consequently, the framework achieved a robust overall accuracy of 85.18% (Kappa = 0.83), comparable to the 81.25% accuracy reported in Guo et al.'s research [42], thus ensuring high-quality input for subsequent carbon modeling.

In terms of carbon estimation, the model yielded a satisfactory performance (R^2 = 0.7057; RMSE = 13.35 Mg ha^{-1}). The synergy of Sentinel-1 SAR and Sentinel-2 optical data aligns with the theoretical consensus in recent remote sensing research, which establishes that such multi-source integration effectively mitigates saturation issues common in subtropical forests [43,44]. The result is comparable to recent pixel-level estimations (10 m) in heterogeneous landscapes, where R^2 values range from 0.65 to 0.75 [45]. Crucially, a key distinction of this study lies in its taxonomic resolution. While most existing infrastructure monitoring projects rely on broad forest functional types [46–48], the developed framework in this research accomplished high-precision species-level mapping. This granularity enabled the detection of subtle population variations, such as the specific resurgence of *P. massoniana* amidst a general decline, that would be obscured in coarser classification systems.

The temporal transferability of models poses a crucial challenge in retrospective analysis. In the retrospective analysis of historical imagery, the utilization of models trained with contemporary data and the integration of corrected data constitute a well-established methodology in remote-sensing vegetation monitoring [49]. In this study, the application of the model trained with 2024 field data for 2019 and 2022 images is supported by rigorous radiometric and data-range controls. First, atmospherically corrected Sentinel-2 Level-2A products and restricted imagery to the same phenological window (September–October) were utilized to minimize spectral drift. More importantly, the 2024 field survey was designed to cover a broad spectrum of forest conditions, encompassing mature, high-biomass stands. The pixel-level AGC density in the training dataset reaches a maximum of 132.004 Mg ha^{-1}. Our analysis reveals that the predicted AGC values for historical years (2019 and 2022) are primarily concentrated below 60 Mg ha^{-1}. Since these historical estimates fall well within the upper limit of the training domain, the retrospective analysis relies on valid interpolation within a learned feature space rather than risky extrapolation [50]. Despite these robust controls, in the absence of independent historical validation, the reported AGC values were regarded as estimates subject to model uncertainty stemming from the validation RMSE. While the absolute values contain inherent uncertainties, the relative spatiotemporal trends, specifically the divergence between the Environmental

Impact Area (EIA) and the Ecological Buffer Area (EBA), remain statistically robust indicators of green engineering impacts, and the results provide reliable indicators for regional carbon dynamics assessment.

4.2. Spatial–Temporal Evolution of AGC Under Green Engineering Intervention

The spatial–temporal evolution of AGC within the Pinglu Canal Basin mirrors the interactive dynamics between construction-related activities and vegetation replanting initiatives. Spatial variation in AGC reflected the contrasting disturbance intensities and recovery patterns between the EBA and EIA. The EIA functioned as the principal disturbance core, where extensive excavation and vegetation clearance coincided with concentrated carbon depletion. In contrast, the EBA mainly experienced indirect effects, leading to a more diffuse and moderate AGC decline. The sharp decline in the EIA (28.91%), contrasting with the relative stability in the EBA, is spatially and temporally consistent with the intensification of engineering activities. The spatial heterogeneity of AGC is also driven by the distinct physiological and ecological traits of dominant tree species [51]. Broadleaved species, particularly *E. grandis*, exhibit rapid growth rates and high carbon sequestration efficiency, enabling them to accumulate biomass quickly in short rotation cycles. This physiological advantage explains their dominance in the high-carbon zones of the EBA. In contrast, coniferous species like *P. massoniana* generally possess slower growth rates and lower wood density, contributing less to the immediate carbon pool but offering greater disturbance resistance in oligotrophic soils. The spatial differentiation demonstrates a hierarchical recovery mechanism, where the EIA requires targeted soil rehabilitation and reforestation, while the EBA acts as a buffer sustaining ecological continuity [52]. These results confirm that carbon dynamics under green engineering exhibit both spatial heterogeneity and temporal lag, highlighting the imperative of formulating restoration strategies tailored to specific disturbance gradients [53].

The species-level trajectories revealed highlight a functional re-allocation of carbon sinks. *E. grandis*, serving as the primary carbon carrier, experienced a continuous decline and accounted for the majority of the cumulative carbon loss, reflecting their vulnerability to harvesting cycles and land clearing. In contrast, *P. massoniana* exhibited a distinct resilience and recovery capability. After an initial decline during the early construction phase (2019–2022), AGC stocks of *P. massoniana* in both the EBA and EIA showed a notable rebound in the later phase (2022–2024), absorbing a significant portion of the carbon gain. The recovery trajectory aligns with the implementation of green engineering initiatives, which prioritized the replanting of native coniferous and broadleaved species over short-rotation monocultures to enhance long-term ecosystem stability and resilience. These contrasting patterns illustrate a strategic trade-off. While plantation-dominated ecosystems (fast-growing species) provide rapid initial biomass accumulation, they exhibit limited persistence under disturbance [54]. Conversely, the increasing share of native species supports long-term sustainability [55]. Therefore, the observed compositional shift marks a transition toward a more balanced, resilient, and diversified carbon pool.

4.3. Carbon Sequestration Benefits and Management Strategies

The spatiotemporal trajectory of AGC along the Pinglu Canal indicates that green engineering can effectively mitigate the ecological costs associated with infrastructure construction by facilitating vegetation restoration and carbon replenishment. During the period from 2019 to 2024, the total loss of AGC in the canal basin amounted to 16.88%. However, unlike traditional gray infrastructure projects which typically incur permanent carbon loss [48], the green engineering initiatives in Pinglu Canal showed that restoration efforts, such as reforestation, slope stabilization, and compensatory afforestation, effectively

offset 34.45% of the cumulative loss at the species level. These findings confirm that green engineering not only limits initial carbon depletion but also establishes a quantifiable pathway for rapid recovery. While short-term AGC recovery was clearly observed under these interventions, full recovery has not yet been achieved. This underscores that continuous management and long-term ecological succession are essential prerequisites for ensuring lasting carbon stability [56].

The influence of species composition adjustments on carbon storage emphasizes that forest recovery driven by engineering is not merely about replenishing biomass but also involves a structural reorganization of carbon sources in response to the disturbance gradients induced by construction [57]. In engineered landscapes like canal corridors, species-level carbon assessment is crucial for discerning differential responses to disturbance and restoration [58]. From a management perspective, the success of ecological restoration projects hinges on the implementation of targeted and adaptive carbon management strategies. Prioritizing mixed forests over monoculture plantations not only facilitates rapid carbon sequestration but also enhances the structural resilience of the ecosystem [59].

Moreover, long-term management mechanisms, including rotational thinning, enrichment planting of native species, and multi-species slope revegetation, are indispensable for maintaining the carbon sequestration potential of the canal corridor [60,61]. Ultimately, the Pinglu Canal case demonstrates that green engineering can transform infrastructure from a carbon-emitting process into a managed ecological system capable of progressive carbon recovery and biodiversity enhancement. Integrating species-level carbon metrics into restoration frameworks enables an accurate evaluation of project efficacy, providing robust scientific evidence to guide adaptive ecosystem restoration in future large-scale infrastructure developments.

4.4. Limitations and Future Directions

Although this study provides novel insights into the species-level carbon responses and recovery dynamics under green engineering interventions, several limitations warrant attention. First, the temporal scope (2019–2024) encompasses only the pre-construction, early construction, mid-construction, and early restoration phases of the Pinglu Canal project. This limited timeframe cannot fully represent the complete successional trajectory of forest carbon restoration. Long-term monitoring is essential for capturing the delayed recovery and carbon stabilization processes that typically occur following infrastructure disturbances [62]. This monitoring can offer data to support the scientific assessment of the ecological benefits of green engineering.

Second, the AGC estimation relied primarily on Sentinel-1/2 data combined with limited ground-based calibration. While the random forest model achieved satisfactory accuracy, uncertainties may persist due to optical-band saturation in high-biomass stands and limited vertical-structure sensitivity. Integrating airborne or spaceborne LiDAR (e.g., GEDI or ICESat-2) with hyperspectral data to construct species-specific carbon storage models can further enhance the characterization of canopy structure and the generalization capacity of the models [63]. In particular, the emerging hyperspectral LiDAR is more conducive to accurately interpreting tree species types and carbon storage from a three-dimensional spectral and structural perspective [64,65]. This more effectively unveils the ecological mechanism between tree species composition and carbon storage.

Third, regarding causal attribution, this study relied on the comparison between the Environmental Impact Area (EIA) and the Ecological Buffer Area (EBA). This design does not strictly isolate engineering impacts from regional background drivers as robustly as a formal Before–After–Control–Impact (BACI) design with independent control basins [66]. To overcome this limitation and further resolve the complex mechanisms driving carbon

dynamics, future research should integrate project redline spatial constraints with land use transition matrices to construct a multi-factor attribution analysis model. This framework will aim to quantitatively decouple the independent contribution rates of engineering construction (e.g., permanent land occupation), forest management practices, natural vegetation growth, and ecological restoration initiatives to carbon storage changes. Such a mechanistic decomposition is essential for precise carbon accountability and adaptive management in large-scale infrastructure projects.

Finally, this study focused mainly on aboveground carbon stocks, whereas a complete assessment of ecosystem carbon dynamics should incorporate belowground carbon, soil organic carbon, and other co-benefits such as biodiversity recovery, soil stability, and hydrological regulation [67]. Future research should link these indicators with AGC dynamics and enable a more holistic assessment of ecological performance in green engineering projects.

5. Conclusions

This study quantified the spatiotemporal dynamics of aboveground carbon (AGC) at the tree species level across the Pinglu Canal Basin under green engineering initiatives. By synergizing Sentinel-1 Synthetic Aperture Radar (SAR) and Sentinel-2 multispectral data, the framework achieved refined tree species mapping with an overall accuracy of 85.18% (Kappa = 0.8319) and reliable AGC estimation (R^2 = 0.7057; RMSE = 13.35 Mg ha^{-1}) at a 10 m resolution. The results revealed that from 2019 to 2024, the total aboveground carbon (AGC) in the Pinglu Canal Basin declined by 16.88%, a trend spatiotemporally coinciding with the intensification of construction activities. Spatial heterogeneity was pronounced and the Environmental Impact Area (EIA) functioned as the primary disturbance core characterized by rapid carbon depletion, whereas the broader Ecological Buffer Area (EBA) acted as a regional carbon stabilizer.

At the tree species level, divergent trajectories were observed. *Eucalyptus grandis* plantations accounted for the majority of the cumulative carbon loss, reflecting their vulnerability to harvesting and clearing. In contrast, *Pinus massoniana* exhibited a resilience-driven rebound in the mid-construction phase (2022–2024), while *Litchi chinensis* and other native species demonstrated steady gains. Cumulatively, these species-specific carbon gains associated with natural growth and restoration initiatives effectively offset 34.45% of the carbon loss across the basin. In addition, the compositional shift from *Eucalyptus*-dominated monocultures to a more diversified forest structure reflects a reorganization toward a balanced and resilient carbon pool.

These findings demonstrate that green engineering has the potential to transform infrastructure development from a carbon-intensive source into a managed ecosystem capable of progressive recovery. Crucially, the proposed framework provides a scalable, high-precision monitoring tool to quantify the efficacy of ecological restoration and forest conservation, thereby directly supporting the United Nations Sustainable Development Goal 15 (Life on Land) targets for sustainable forest management.

Future research should aim to refine causal attribution by integrating project redline spatial constraints with land use transition matrices. Constructing a multi-factor attribution model will allow for the quantitative decoupling of the independent contributions of engineering construction, forest management, and natural growth to carbon dynamics. Furthermore, extending the monitoring timeframe and incorporating LiDAR data will be essential to fully characterize the long-term successional trajectory of the recovering carbon pool.

Author Contributions: Conceptualization, W.W. (Wenhuan Wang) and Y.W.; methodology, W.W. (Wenhuan Wang); software, W.W. (Wenqian Wu) and J.B.; validation, W.W. (Wenhuan Wang) and D.H.; formal analysis, W.W. (Wenhuan Wang); investigation, W.W. (Wenhuan Wang), W.Z. and

W.X.; data curation, W.W. (Wenqian Wu); writing—original draft preparation, W.W. (Wenhuan Wang); writing—review and editing, W.W. (Wenhuan Wang) and W.Z.; visualization, J.B. and D.H.; supervision, W.Z.; funding acquisition, Y.W. All authors have read and agreed to the published version of the manuscript.

Funding: This research was funded by the Guangxi Science and Technology Major Program (Grant No. GUIKEAA23062054), Open Research Project of the Key Laboratory of China-ASEAN Satellite Remote Sensing Applications, Ministry of Natural Resources of the People's Republic of China (Grant No. KLCARS-2025-G04), and the National Natural Science Foundation of China (NSFC) (Grant No. 42501432).

Data Availability Statement: The data presented in this study are available on request from the corresponding author.

Conflicts of Interest: The authors declare no conflicts of interest.

References

1. Pan, Y.; Birdsey, R.A.; Fang, J.; Houghton, R.; Kauppi, P.E.; Kurz, W.A.; Phillips, O.L.; Shvidenko, A.; Lewis, S.L.; Canadell, J.G.; et al. A large and persistent carbon sink in the world's forests. *Science* **2011**, *333*, 988–993. [CrossRef] [PubMed]
2. IPCC. *Climate Change and Land: An IPCC Special Report on Climate Change, Desertification, Land Degradation, Sustainable Land Management, Food Security, and Greenhouse Gas Fluxes in Terrestrial Ecosystems*; Intergovernmental Panel on Climate Change: Geneva, Switzerland, 2019.
3. Noulekoun, F.; Mensah, S.; Kim, H.; Jo, H.; Gouwakinnou, G.N.; Houehanou, T.D.; Mensah, M.; Naab, J.; Son, Y.; Khamzina, A. Tree size diversity is the major driver of aboveground carbon storage in dryland agroforestry parklands. *Sci. Rep.* **2023**, *13*, 22210. [CrossRef] [PubMed]
4. Shen, F.; Haseeb, M.; Tahir, Z.; Mahmood, S.A.; Tariq, A. Reimagining land use policies: Carbon trade-offs between urbanization and ecological restoration. *Land Use Policy* **2025**, *158*, 107770. [CrossRef]
5. Babar, M.A.; Shaha, M.R.D. A review paper on principles of green engineering. *Int. J. Eng. Appl. Sci. Technol.* **2024**, *9*, 112–114. [CrossRef]
6. Information Office of the People's Government of Guangxi Zhuang Autonomous Region. *Guangxi Accelerates the Construction of Major Infrastructure and Builds the Pinglu Canal with High Standards and Quality*; Information Office of the People's Government of Guangxi Zhuang Autonomous Region: Nanning, China, 2024.
7. Guangxi Zhuang Autonomous Region Department of Ecology and Environment. *Special Action Plan for Green Engineering of the Pinglu Canal*; Guangxi Zhuang Autonomous Region Department of Ecology and Environment: Nanning, China, 2023.
8. Rodríguez-Veiga, P.; Wheeler, J.; Louis, V.; Tansey, K.; Balzter, H. Quantifying Forest Biomass Carbon Stocks from Space. *Curr. For. Rep.* **2017**, *3*, 1–18. [CrossRef]
9. Issa, S.; Dahy, B.; Ksiksi, T.; Saleous, N. A Review of Terrestrial Carbon Assessment Methods Using Geo-Spatial Technologies with Emphasis on Arid Lands. *Remote Sens.* **2020**, *12*, 2008. [CrossRef]
10. Chen, Y.; Feng, X.; Fu, B.; Ma, H.; Zohner, C.M.; Crowther, T.W.; Huang, Y.; Wu, X.; Wei, F. Maps with 1 km resolution reveal increases in above- and belowground forest biomass carbon pools in China over the past 20 years. *Earth Syst. Sci. Data* **2023**, *15*, 897–910. [CrossRef]
11. Santoro, M.; Cartus, O.; Carvalhais, N.; Rozendaal, D.M.A.; Avitabile, V.; Araza, A.; de Bruin, S.; Herold, M.; Quegan, S.; Rodríguez-Veiga, P.; et al. The global forest above-ground biomass pool for 2010 estimated from high-resolution satellite observations. *Earth Syst. Sci. Data* **2021**, *13*, 3927–3950. [CrossRef]
12. Potapov, P.; Li, X.; Hernandez-Serna, A.; Tyukavina, A.; Hansen, M.C.; Kommareddy, A.; Pickens, A.; Turubanova, S.; Tang, H.; Silva, C.E.; et al. Mapping global forest canopy height through integration of GEDI and Landsat data. *Remote Sens. Environ.* **2021**, *253*, 112165. [CrossRef]
13. Gonzalez, P.; Asner, G.P.; Battles, J.J.; Lefsky, M.A.; Waring, K.M.; Palace, M. Forest carbon densities and uncertainties from Lidar, QuickBird, and field measurements in California. *Remote Sens. Environ.* **2010**, *114*, 1561–1575. [CrossRef]
14. Ghamisi, P.; Gloaguen, R.; Atkinson, P.M.; Benediktsson, J.A.; Rasti, B.; Yokoya, N.; Wang, Q.; Hofle, B.; Bruzzone, L.; Bovolo, F.; et al. Multisource and Multitemporal Data Fusion in Remote Sensing: A Comprehensive Review of the State of the Art. *IEEE Geosci. Remote Sens. Mag.* **2019**, *7*, 6–39. [CrossRef]
15. Zhu, N.N.; Yang, B.S.; Dong, Z. A novel framework for forest vegetation carbon stock estimation based on remote sensing. *Natl. Remote Sens. Bull.* **2025**, *29*, 134–146.
16. Jiang, W.; Zhang, L.; Zhang, X.; Gao, S.; Gao, H.; Sun, L.; Yan, G. Multi-Decision Vector Fusion Model for Enhanced Mapping of Aboveground Biomass in Subtropical Forests Integrating Sentinel-1, Sentinel-2, and Airborne LiDAR Data. *Remote Sens.* **2025**, *17*, 1285. [CrossRef]

17. Talukdar, S.; Singha, P.; Mahato, S.; Shahfahad; Pal, S.; Liou, Y.; Rahman, A. Land-Use Land-Cover Classification by Machine Learning Classifiers for Satellite Observations—A Review. *Remote Sens.* **2020**, *12*, 1135. [CrossRef]
18. Chen, C.; Da Qi, Y.; Qin, Z.; Li, Y.; Li, Y. Pine wood species identification based on random forest transformer and near infrared spectroscopy. *Talanta* **2026**, *297*, 128599. [CrossRef]
19. Suárez-Fernández, G.E.; Martínez-Sánchez, J.; Arias, P. Enhancing carbon stock estimation in forests: Integrating multi-data predictors with random forest method. *Ecol. Inform.* **2025**, *86*, 102997. [CrossRef]
20. Tian, S.; Sha, A.; Luo, Y.; Ke, Y.; Spencer, R.; Hu, X.; Ning, M.; Zhao, Y.; Deng, R.; Gao, Y.; et al. A novel framework for river organic carbon retrieval through satellite data and machine learning. *ISPRS-J. Photogramm. Remote Sens.* **2025**, *221*, 109–123. [CrossRef]
21. Li, H.; Hiroshima, T.; Li, X.; Hayashi, M.; Kato, T. High-resolution mapping of forest structure and carbon stock using multi-source remote sensing data in Japan. *Remote Sens. Environ.* **2024**, *312*, 114322. [CrossRef]
22. Li, Z.; Bi, S.; Hao, S.; Cui, Y. Aboveground biomass estimation in forests with random forest and Monte Carlo-based uncertainty analysis. *Ecol. Indic.* **2022**, *142*, 109246. [CrossRef]
23. Wang, Z.; Gong, H.; Huang, M.; Gu, F.; Wei, J.; Guo, Q.; Song, W. A multimodel random forest ensemble method for an improved assessment of Chinese terrestrial vegetation carbon density. *Methods Ecol. Evol.* **2023**, *14*, 117–132. [CrossRef]
24. Jung, J.; Kim, S.; Hong, S.; Kim, K.; Kim, E.; Im, J.; Heo, J. Effects of national forest inventory plot location error on forest carbon stock estimation using k-nearest neighbor algorithm. *ISPRS-J. Photogramm. Remote Sens.* **2013**, *81*, 82–92. [CrossRef]
25. Lee, T.R.; Wood, W.T.; Phrampus, B.J. A Machine Learning (kNN) Approach to Predicting Global Seafloor Total Organic Carbon. *Glob. Biogeochem. Cycles* **2019**, *33*, 37–46. [CrossRef]
26. Campbell, M.J.; Eastburn, J.F.; Dennison, P.E.; Vogeler, J.C.; Stovall, A.E.L. Evaluating the performance of airborne and spaceborne lidar for mapping biomass in the United States' largest dry woodland ecosystem. *Remote Sens. Environ.* **2024**, *308*, 114196. [CrossRef]
27. Yuan, Y.; Guo, W.; Tang, S.; Zhang, J. Effects of patterns of urban green-blue landscape on carbon sequestration using XGBoost-SHAP model. *J. Clean. Prod.* **2024**, *476*, 143640. [CrossRef]
28. Cheng, F.; Ou, G.; Wang, M.; Liu, C. Remote Sensing Estimation of Forest Carbon Stock Based on Machine Learning Algorithms. *Forests* **2024**, *15*, 681. [CrossRef]
29. Arantes, A.E.; Ferreira, L.G.; Coe, M.T. The seasonal carbon and water balances of the Cerrado environment of Brazil: Past, present, and future influences of land cover and land use. *ISPRS-J. Photogramm. Remote Sens.* **2016**, *117*, 66–78. [CrossRef]
30. Wu, Y.; Zheng, J.; Gao, J.; He, X.; Liu, X. Functional Diversity Explains Ecosystem Carbon Storage in Subtropical Forests. *Glob. Change Biol.* **2025**, *31*, e70120. [CrossRef]
31. Xu, H.; Yue, C.; Zhang, Y.; Liu, D.; Piao, S. Forestation at the right time with the right species can generate persistent carbon benefits in China. *Proc. Natl. Acad. Sci. USA* **2023**, *120*, e1989979176. [CrossRef]
32. Bai, Y.; Pang, Y.; Kong, D. Integrating remote sensing and 3-PG model to simulate the biomass and carbon stock of *Larix olgensis* plantation. *For. Ecosyst.* **2024**, *11*, 100213. [CrossRef]
33. Kunert, N.; El-Madany, T.S.; Aparecido, L.M.T.; Wolf, S.; Potvin, C. Understanding the controls over forest carbon use efficiency on small spatial scales: Effects of forest disturbance and tree diversity. *Agric. For. Meteorol.* **2019**, *269–270*, 136–144. [CrossRef]
34. Li, F.; Jia, Z.; Zhou, X. Establishing Natural Resources Monitoring Systems in China: Situation, Problem and Suggestion. *Int. Arch. Photogramm. Remote Sens. Spat. Inf. Sci.* **2024**, *XLVIII-4-2024*, 599–606. [CrossRef]
35. Zhao, Y.; Guo, F.; Wang, Y.; Huang, J.; Peng, D. Estimating Forest Growing Stock Volume Using Feature Selection and Advanced Remote Sensing Algorithm. *Remote Sens. Appl. Soc. Environ.* **2025**, *37*, 101458. [CrossRef]
36. Drusch, M.; Del Bello, U.; Carlier, S.; Colin, O.; Fernandez, V.; Gascon, F.; Hoersch, B.; Isola, C.; Laberinti, P.; Martimort, P.; et al. Sentinel-2: ESA's Optical High-Resolution Mission for GMES Operational Services. *Remote Sens. Environ.* **2012**, *120*, 25–36. [CrossRef]
37. Torres, R.; Snoeij, P.; Geudtner, D.; Bibby, D.; Davidson, M.; Attema, E.; Potin, P.; Rommen, B.; Floury, N.; Brown, M.; et al. GMES Sentinel-1 mission. *Remote Sens. Environ.* **2012**, *120*, 9–24. [CrossRef]
38. Ma, M.; Liu, J.; Liu, M.; Zeng, J.; Li, Y. Tree Species Classification Based on Sentinel-2 Imagery and Random Forest Classifier in the Eastern Regions of the Qilian Mountains. *Forests* **2021**, *12*, 1736. [CrossRef]
39. *GB/T 43648-2024*; State Administration for Market Regulation; Standardization Administration of the People's Republic of China; Tree Biomass Models and Related Parameters to Carbon Accounting for Major Tree Species. Standards Press of China: Beijing, China, 2024.
40. Xu, W.; Cheng, Y.; Luo, M.; Mai, X.; Wang, W.; Zhang, W.; Wang, Y. Progress and Limitations in Forest Carbon Stock Estimation Using Remote Sensing Technologies: A Comprehensive Review. *Forests* **2025**, *16*, 449. [CrossRef]
41. Dong, H.; Tang, L.; Liu, J.; Hu, X.; Shao, G. Remote sensing of urban tree carbon stocks: A methodological review. *ISPRS-J. Photogramm. Remote Sens.* **2025**, *227*, 570–593. [CrossRef]
42. Guo, H.; Boonprong, S.; Wang, S.; Zhang, Z.; Liang, W.; Xu, M.; Yang, X.; Wang, K.; Li, J.; Gao, X.; et al. Dominant Tree Species Mapping Using Machine Learning Based on Multi-Temporal and Multi-Source Data. *Remote Sens.* **2024**, *16*, 4674. [CrossRef]
43. Taşkın, G.; Kaya, H.; Bruzzone, L. Feature Selection Based on High Dimensional Model Representation for Hyperspectral Images. *IEEE Trans. Image Process.* **2017**, *26*, 2918–2928. [CrossRef]

44. Qadeer, A.; Shakir, M.; Wang, L.; Talha, S.M. Evaluating machine learning approaches for aboveground biomass prediction in fragmented high-elevated forests using multi-sensor satellite data. *Remote Sens. Appl. Soc. Environ.* **2024**, *36*, 101291. [CrossRef]
45. Zhou, J.; Zan, M.; Zhai, L.; Yang, S.; Xue, C.; Li, R.; Wang, X. Remote sensing estimation of aboveground biomass of different forest types in Xinjiang based on machine learning. *Sci. Rep.* **2025**, *15*, 6187. [CrossRef]
46. Xu, W.; Mai, X.; Deng, S.; Wang, W.; Wu, W.; Zhang, W.; Wang, Y. High-Resolution Mapping and Impact Assessment of Forest Aboveground Carbon Stock in the Pinglu Canal Basin: A Multi-Sensor and Multi-Model Machine Learning Approach. *Forests* **2025**, *16*, 1130. [CrossRef]
47. Wang, Y.; Cong, N.; Zhong, Y.; Fu, Y.; Wang, N.; Ouyang, L.; Yao, W. Impacts of cascade dam construction on riparian vegetation in an alpine region. *J. Hydrol.* **2025**, *652*, 132665. [CrossRef]
48. Dullah, H.; Malek, M.A.; Omar, H.; Mangi, S.A.; Hanafiah, M.M. Assessing changes of carbon stock in dipterocarp forest due to hydro-electric dam construction in Malaysia. *Environ. Sci. Pollut. Res.* **2021**, *28*, 44264–44276. [CrossRef] [PubMed]
49. Main-Knorn, M.; Cohen, W.B.; Kennedy, R.E.; Grodzki, W.; Pflugmacher, D.; Griffiths, P.; Hostert, P. Monitoring coniferous forest biomass change using a Landsat trajectory-based approach. *Remote Sens. Environ.* **2013**, *139*, 277–290. [CrossRef]
50. Ploton, P.; Mortier, F.; Réjou-Méchain, M.; Barbier, N.; Picard, N.; Rossi, V.; Dormann, C.; Cornu, G.; Viennois, G.; Bayol, N.; et al. Spatial validation reveals poor predictive performance of large-scale ecological mapping models. *Nat. Commun.* **2020**, *11*, 4540. [CrossRef]
51. Mensah, S.; Salako, V.K.; Seifert, T. Structural complexity and large-sized trees explain shifting species richness and carbon relationship across vegetation types. *Funct. Ecol.* **2020**, *34*, 1731–1745. [CrossRef]
52. Qiu, S.; Yu, Q.; Niu, T.; Fang, M.; Guo, H.; Liu, H.; Li, S.; Zhang, J. Restoration and renewal of ecological spatial network in mining cities for the purpose of enhancing carbon Sinks: The case of Xuzhou, China. *Ecol. Indic.* **2022**, *143*, 109313. [CrossRef]
53. Li, S.; Yang, P.; Yang, C.; Zhang, H.; Gao, X. The Impact of Ecological Restoration Measures on Carbon Storage: Spatio-Temporal Dynamics and Driving Mechanisms in Karst Desertification Control. *Land* **2025**, *14*, 1903. [CrossRef]
54. Hua, F.; Bruijnzeel, L.A.; Meli, P.; Martin, P.A.; Zhang, J.; Nakagawa, S.; Miao, X.; Wang, W.; McEvoy, C.; Peña-Arancibia, J.L.; et al. The biodiversity and ecosystem service contributions and trade-offs of forest restoration approaches. *Science* **2022**, *376*, 839–844. [CrossRef]
55. Osuri, A.M.; Gopal, A.; Raman, T.R.S.; DeFries, R.; Cook-Patton, S.C.; Naeem, S. Greater stability of carbon capture in species-rich natural forests compared to species-poor plantations. *Environ. Res. Lett.* **2020**, *15*, 34011. [CrossRef]
56. Chen, Y.; Hu, B.; Tang, J.; Wang, Y. Comprehensive consolidation and ecological restoration projects drive the variation of ecosystem services and their terrain gradient effect in Jiangxi Province, China. *Ecol. Eng.* **2025**, *220*, 107728. [CrossRef]
57. Magnabosco Marra, D.; Trumbore, S.E.; Higuchi, N.; Ribeiro, G.H.P.M.; Negrón Juárez, R.I.; Holzwarth, F.; Rifai, S.W.; Dos Santos, J.; Lima, A.J.N.; Kinupp, V.F.; et al. Windthrows control biomass patterns and functional composition of Amazon forests. *Glob. Change Biol.* **2018**, *24*, 5867–5881. [CrossRef] [PubMed]
58. Pires Coelho, A.J.; Ribeiro Matos, F.A.; Villa, P.M.; Heringer, G.; Pontara, V.; de Paula Almado, R.; Alves Meira-Neto, J.A. Multiple drivers influence tree species diversity and above-ground carbon stock in second-growth Atlantic forests: Implications for passive restoration. *J. Environ. Manag.* **2022**, *318*, 115588. [CrossRef]
59. Warner, E.; Cook-Patton, S.C.; Lewis, O.T.; Brown, N.; Koricheva, J.; Eisenhauer, N.; Ferlian, O.; Gravel, D.; Hall, J.S.; Jactel, H.; et al. Young mixed planted forests store more carbon than monocultures—A meta-analysis. *Front. For. Glob. Change* **2023**, *6*, 1226514. [CrossRef]
60. Diaz-Balteiro, L.; Rodriguez, L.C.E. Optimal rotations on Eucalyptus plantations including carbon sequestration—A comparison of results in Brazil and Spain. *For. Ecol. Manag.* **2006**, *229*, 247–258. [CrossRef]
61. Benítez, G.; Ruelas-Monjardín, L.C.; Von Thaden, J.; Acosta-Rosado, I.; Alvarado-Castillo, G.; Equihua, M. Carbon storage in a peri-urban neotropical forest: Assessing its potential and patterns of change over half a century. *Urban For. Urban Green.* **2023**, *86*, 128009. [CrossRef]
62. Bustamante, M.M.C.; Roitman, I.; Aide, T.M.; Alencar, A.; Anderson, L.O.; Aragao, L.; Asner, G.P.; Barlow, J.; Berenguer, E.; Chambers, J.; et al. Toward an integrated monitoring framework to assess the effects of tropical forest degradation and recovery on carbon stocks and biodiversity. *Glob. Change Biol.* **2016**, *22*, 92–109. [CrossRef]
63. Duncanson, L.; Kellner, J.R.; Armston, J.; Dubayah, R.; Minor, D.M.; Hancock, S.; Healey, S.P.; Patterson, P.L.; Saarela, S.; Marselis, S.; et al. Aboveground biomass density models for NASA's Global Ecosystem Dynamics Investigation (GEDI) lidar mission. *Remote Sens. Environ.* **2022**, *270*, 112845. [CrossRef]
64. Bai, J.; Niu, Z.; Wang, L. A theoretical demonstration on the independence of distance and incidence angle effects for small-footprint hyperspectral LiDAR: Basic physical concepts. *Remote Sens. Environ.* **2024**, *315*, 114452. [CrossRef]
65. Bai, J.; Niu, Z.; Huang, Y.; Bi, K.; Fu, Y.; Gao, S.; Wu, M.; Wang, L. Full-waveform hyperspectral LiDAR data decomposition via ranking central locations of natural target echoes (Rclonte) at different wavelengths. *Remote Sens. Environ.* **2024**, *310*, 114227. [CrossRef]

66. Meroni, M.; Schucknecht, A.; Fasbender, D.; Rembold, F.; Fava, F.; Mauclaire, M.; Goffner, D.; Di Lucchio, L.M.; Leonardi, U. Remote sensing monitoring of land restoration interventions in semi-arid environments with a before–after control-impact statistical design. *Int. J. Appl. Earth Obs. Geoinf.* **2017**, *59*, 42–52.
67. Zhai, T.; Chang, M.; Ma, Y.; Huang, L.; Li, L. Exploring the changes and driving mechanisms in the production-transport-consumption process of ecosystem services flow in the Yellow River Basin under the background of policy changes. *Ecol. Indic.* **2023**, *151*, 110316. [CrossRef]

Disclaimer/Publisher's Note: The statements, opinions and data contained in all publications are solely those of the individual author(s) and contributor(s) and not of MDPI and/or the editor(s). MDPI and/or the editor(s) disclaim responsibility for any injury to people or property resulting from any ideas, methods, instructions or products referred to in the content.